Research Article Vol. 13, No. 12 / 1 Dec 2023 / *Optical Materials Express* 3416

Optical Materials EXPRESS

Computationally-driven discovery of second harmonic generation in $EuBa_3(B_3O_6)_3$ through inversion symmetry breaking

JINGYANG HE,[1,†] LOUIS ALAERTS,[2,†] YU WANG,[3,4,†] VICTOR TRINQUET,[5] SUGURU YOSHIDA,[3,4] HEMANT YENNAWAR,[6] VICTOR SANNI,[2] ROMAIN CLAES,[5] ROWAN KATZBAER,[7] EVAN KRYSKO,[3] SAUGATA SARKER,[1] RAYMOND E. SCHAAK,[7,8,9] GIAN-MARCO RIGNANESE,[5] GEOFFROY HAUTIER,[2,10] ZHIQIANG MAO,[3,4,11] AND VENKATRAMAN GOPALAN[1,3,12]

[1] *Department of Materials Science and Engineering, Pennsylvania State University, University Park, PA, 16802, USA*
[2] *Thayer School of Engineering, Dartmouth College, Hanover, NH, 03755, USA*
[3] *Department of Physics, Pennsylvania State University, University Park, PA, 16802, USA*
[4] *2D Crystal Consortium, Materials Research Institute, Pennsylvania State University, University Park, PA, 16802, USA*
[5] *Institute of Condensed Matter and Nanosciences, UCLouvain, 1348 Louvain-la-Neuve, Belgium*
[6] *Department of Biochemistry & Molecular Biology, Pennsylvania State University, University Park, PA, 16802, USA*
[7] *Department of Chemistry, Pennsylvania State University, University Park, PA, 16802, USA*
[8] *Department of Chemical Engineering, Pennsylvania State University, University Park, PA, 16802, USA*
[9] *Materials Research Institute, Pennsylvania State University, University Park, PA, 16802, USA*
[10] *geoffroy.hautier@dartmouth.edu*
[11] *zim1@psu.edu*
[12] *vxg8@psu.edu*
[†] Equal contribution

Abstract: Nonlinear optical (NLO) crystals with superior properties are significant for advancing laser technologies and applications. Introducing rare earth metals to borates is a promising and effective way to modify the electronic structure of a crystal to improve its optical properties in the visible and ultraviolet range. In this work, we computationally discover inversion symmetry breaking in $EuBa_3(B_3O_6)_3$, which was previously identified as centric, and demonstrate noncentrosymmetry via synthesizing single crystals for the first time by the floating zone method. We determine the correct space group to be $P\bar{6}$. The material has a large direct bandgap of 5.56 eV and is transparent down to 250 nm. The complete anisotropic linear and nonlinear optical properties were also investigated with a d_{11} of ~0.52 pm/V for optical second harmonic generation. Further, it is Type I and Type II phase matchable. This work suggests that rare earth metal borates are an excellent crystal family for exploring future deep ultraviolet (DUV) NLO crystals. It also highlights how first principles computations combined with experiments can be used to identify noncentrosymmetric materials that have been wrongly assigned to be centrosymmetric.

1. Introduction

Nonlinear optical (NLO) crystals are the essential components of high-power lasers for generating ultraviolet (UV) light, especially the UV-C range, defined as 200–280 nm [1]. It has a variety of technological applications such as lithography, [2,3] micromachining, [4] and spectroscopy

#497727
Journal © 2023

https://doi.org/10.1364/OME.497727
Received 9 Jun 2023; revised 30 Sep 2023; accepted 17 Oct 2023; published 6 Nov 2023

[5]. The wavelengths of interest are obtained using frequency conversion through nonlinear optical phenomena such as second harmonic generation (SHG) and sum frequency generation (SFG). Generally, a good UV NLO crystal should satisfy the following requirements: large second-order nonlinearity (large SHG tensor coefficients), broad UV transparency window, phase matchability, high laser damage threshold (LDT) values, and easy synthesis. It is well-known that bandgaps and nonlinear susceptibility generally scale inversely; hence, crystals with large bandgaps (and therefore DUV transparency) usually have low nonlinear susceptibility. As a result, ultraviolet NLO crystals typically have lower SHG coefficients as compared to visible and infrared NLO crystals. Since it is difficult to find a material that satisfies all the requirements, researchers are actively looking for new UV crystals and many borate-based NLO materials such as β-BaB_2O_4 (BBO), [6] LiB_3O_5 (LBO), [7] CsB_3O_5 (CBO) [8] and $KBe_2BO_3F_2$ (KBBF) [5] have been discovered and utilized in UV NLO applications. Among these materials, KBBF is the only crystal with efficient frequency conversion below the DUV barrier of 200 nm. Clearly, the rapid development of UV laser applications demands the continuous exploration of new UV NLO crystals.

Borate is considered to be one of the best crystal systems for exploring good UV NLO crystals [6,7]. Because of the significant electronegativity difference in boron and oxygen, the B-O bonds have strong ionic characteristics, giving rise to large bandgaps and low short-cutoff wavelengths. The typical groups formed are planar $[BO_3]$ triangles and $[BO_4]$ tetrahedra. In particular, the planar $[BO_3]$ units contain π-conjugated bonds in which the electrons are delocalized and easily polarized when an electric field is applied, thus giving rise to the strong SHG response. In addition, its planar nature increases the anisotropy and leads to more significant birefringence; thus they are more likely to be phase-matchable. In particular, rare earth borates are a promising crystal system to explore for new UV NLO crystals. Incorporating rare earth metals has several advantages. They have closed-shell or half-filled 4f orbitals; therefore, the d-d and f-f electronic transitions are impeded, which is beneficial for broadening the transparency window [8,9]. Also, because of the complex electronic configuration and the large ionic radius, the rare earth elements will bond with the oxygen ions to form distorted polyhedra, enhancing the overall SHG performance [9].

$EuBa_3(B_3O_6)_3$ (EBBO) is an example of rare earth borate-based crystals with planar $[BO_3]$ triangles, which can be a new UV NLO crystal. In EBBO, three $[BO_3]$ triangles form a planar $[B_3O_6]$ ring. This compound was previously synthesized in the polycrystalline form and reported to crystallize in the non-polar space group $P6_3/m$ [10]. First principles phonon computations identified that this family of materials of formula $XA_3(B_3O_6)_3$ (with X = In, Sc, ... X = Ba, Sr, ... which includes EBBO) present dynamic instabilities and that they should form in a noncentrosymmetric space group. In agreement with the theoretical prediction, we show that EBBO forms indeed in an acentric space group and exhibits an SHG response. We further explore EBBO as a candidate for UV nonlinear photonic applications. We report the first synthesis as well as the linear and nonlinear optical properties of single crystal EBBO and find that EBBO is both Type I and Type II phase-matchable. These findings further confirm that rare earth borate-based crystals are promising for NLO applications and that first principles phonon databases can be used to identify noncentrosymmetric materials with applications in NLO.

2. Experiments

2.1. Polycrystalline crystal synthesis

The polycrystalline EBBO powder was prepared using a solid-state reaction method. We used $BaCO_3$ (Alfa Asar, 99.5%), Eu_2O_3(Alfa Asar, 99.9%), and H_3BO_3 (EMD chemicals, 99.4%) as source materials for the polycrystalline synthesis. Powders of $BaCO_3$, Eu_2O_3, and H_3BO_3 were mixed in a stoichiometric ratio and thoroughly ground in an agate mortar to ensure homogenous mixing. The mixed source material was placed in an Al_2O_3 crucible, heated to 400°C, and held at this temperature for 1 hour to decompose $BaCO_3$ and H_3BO_3. Then the furnace was further heated to 850°C at the rate of 200°C/hour and held at this temperature for 72 hours, followed by turning off the furnace to cool down the material. Powder X-ray diffraction (XRD) analyses showed that the polycrystalline powder synthesized following the above procedures contains a pure EBBO phase.

2.2. Single crystal synthesis

The EBBO single crystals were grown using a floating-zone technique using a commercial image furnace equipped with double-elliptical mirrors (Quantum Design Model: IRF01-001-05). This method consists of melting the bottom end of a feed rod suspended from above and connecting the molten zone to a seed material held from below. The single crystal is continuously grown from the molten solution by lowering both the seed and feed rods.

We used polycrystalline EBBO powder to make feed and seed rods for growing the single crystals. We first ground it into a fine powder in an agate mortar for 30 minutes. An appropriate amount of the powder (10 g) was placed into a clean cylinder-shaped rubber balloon. The balloon loaded with powder was inserted into a quartz tube with a diameter of 11 mm and a length of about 110 mm and compressed in water under a pressure of 60 MPa. After compression, the rubber balloon was carefully cut with scissors. The rod was then sintered at 800 °C for 48 hours in air and cooled to room temperature in the furnace. The seed rod (3 cm in length) was prepared with a similar procedure. In the preparation of the feed and seed rods, we always placed a layer of EBBO powder between the EBBO rod and the Al_2O_3 boat to prevent Al contamination.

To perform the floating-zone crystal growth, the feed rod was suspended from the upper shaft, and the seed rod was mounted on the bottom shaft. Both rods were well aligned along the central axis of the growth chamber (i.e., along the shaft direction). After completing the alignment, we closed the growth chamber and moved the bottom end of the feed rod and the top end of the seed rod to the melting zone with a small gap (~1.5 mm) left between them. Then we flushed the growth chamber by flowing oxygen for 15 minutes and increased the oxygen pressure in the growth chamber up to 4 atm. After the pressure reached 4 atm, we started to ramp up the voltage of the halogen lamps and set the upper and lower shafts to rotate at 14 rpm (The rotation direction is opposite between the upper and lower shafts). The bottom end of the feed rod started to melt at 49 V. When the voltage was increased to 50 V, the bottom end of the feed rod had sufficiently melted. Then we connected the feed rod with the seed rod by slightly moving the bottom shaft upward. After the seed and feed rods were connected, we started the growth, with the growth speed set at 7 mm/h and the feed speed at 30 mm/h. As the growth continued, we adjusted the voltage in the 49–55 V range in terms of the shape of the melt in the melting zone. The best shape is “T”-like for growth. We obtained the “T”-shape melting-zone mostly at 50 V. The growth lasted 5 hours; the crystal rod we obtained at the end was about 30 mm and contained multiple domains. Single domains were obtained by cleaving the crystal rod using a razor blade.

2.3. Linear optical properties

The short-cutoff wavelength was determined by ultraviolet-visible (UV-Vis) spectroscopy (Perkin-Elmer Lambda 950 UV-Vis-NIR Spectrophotometer) and spectroscopic ellipsometry (Woollam M-2000F) at room temperature. The UV-Vis transmittance spectrum was collected on a single crystal EBBO of thickness ~500 µm sample in the range of 250–850 nm with unpolarized light. The ellipsometry data was collected on a polycrystalline pallet from 0.200 µm to 1 µm.

The complex linear optical constants $\tilde{n} = n + ik$ were determined using spectroscopic ellipsometry (Woollam M-2000F). The ellipsometry spectra were collected from 0.200µm to 1µm and fitted to the Cauchy equation $n = A + \frac{B}{\lambda^2} + \frac{C}{\lambda^4}$. The extinction coefficient (describing the absorption) is represented by the Urbach absorption equation $k = k_0 e^{(E-E_o)/E_u}$, where k_0 and E_0 are the characteristic parameters of the material and E_u is the Urbach energy related to the temperature. The absorption coefficient α can be found from k to extract the bandgap of the crystal by the Tauc analysis $(\alpha h\nu)^{1/n} = A(h\nu - E_g)$ [11]. Here, ν is the frequency of the photons and n is 0.5 for direct, and 2 for indirect bandgaps. By plotting $(\alpha h\nu)^{1/n}$ vs. E, one can identify the correct transition and the bandgap by extrapolating the curve to $(\alpha h\nu)^{1/n} = 0$.

2.4. Second harmonic generation (SHG) measurement

The SHG measurement was performed in reflection geometry at normal incidence (i.e. incident laser beam along the surface normal). The 800 nm fundamental laser beam was generated by Spectra-Physics Ti:sapphire (80 fs, 80 MHz) and its polarization was rotated by an angle of ψ using a halfwave plate. Then after passing through an analyzer, the p-polarized ($\|$) and s-polarized ($\perp$) SHG light was detected by a photomultiplier tube. The typical peak power used was around 700 W (pulse energy ~0.056 nJ). The beam diameter was roughly 600 nm. A wedged z-cut $LiNbO_3$ crystal (MTI Corporation) was used as a reference.

2.5. First principle (FP) calculations

The structural optimizations and subsequent self-consistent field calculations were carried out using the Vienna *ab initio* simulation package (VASP) [13–16]. The Perdew-Burke-Ernzerhof generalized-gradient approximation (GGA-PBE) [17] was employed to model the exchange-correlation energy. The projector augmented wave (PAW) method [18] was used, and the wavefunctions were expanded on a plane-wave basis set with a kinetic energy cutoff of 520 eV. Preliminary results showed that explicitly considering the 4-f electrons in the valence leads to a metal. Indeed, these electrons were located around the Fermi level, although a wide bandgap should be present. To address this issue, we tested the Eu_3 VASP pseudopotential with 9 valence electrons ($5p^6\ 5d^1\ 6s^2$), resulting in an indirect gap of ~ 5 eV, and a direct gap of ~5.3 eV. This pseudopotential was therefore adopted. A $3 \times 3 \times 1$ Monkhorst-Pack k-point mesh [19,20] was initially employed to sample the Brillouin zone, and the electronic self-consistent loops were converged to 1×10^{-6} eV of the total energy. The ionic relaxation was considered converged when the force on each atom was below 2 meV/Å. Further calculations with k-points grid of $5 \times 5 \times 1$, energy and forces convergence thresholds of 1×10^{-9} eV and 0.5 meV/Å, respectively, were subsequently performed to obtain a better estimation of the energy differences between the competing phases. Phonons were computed using the density functional perturbation theory (DFPT) as implemented in ABINIT [21,22] and following the procedure used by Petretto *et al.* [23]. The calculations were performed with GGA-PBE functional (considering the f electrons as frozen for the Eu) and a q-point grid of $2 \times 2 \times 2$.

3. Results and discussion

3.1. Material discovery

Starting from a phonon database [12,13] of materials present in the Materials Project [14] and previously synthesized as reported in the Inorganic Crystal Structure Database (ICSD), [15] a family of compounds with general chemical formula $XBa_3B_9O_{18}$ (X = Sc, In,Y, Lu) [10,16–18] and with the centrosymmetric crystal structure ($P6_3/m$) was identified as presenting polar imaginary phonon modes. This is a signature of polar structural instability, which has been used, for instance, to identify a new class of ferroelectric materials [19,20]. Further computations with higher accuracy parameters and using phonons obtained with DFPT confirmed the dynamical instabilities. Among this family, we focus here on EBBO and report its phonon band structure in Fig. 1(a). The centrosymmetric structure is shown in Fig. 1(b) (superposed to a distortion). Dynamical instabilities across the Brillouin zone are present in the phonon band structure, indicating a series of competing distortions (available in Supplement 1), some belonging to polar point groups (Fig. 1(a)). We distorted the structure following all unstable phonons (limiting our distortions to a 2 × 2 × 2 supercell) and subsequently relaxed. Table 1 reports all the distorted structures following this procedure and their energy compared to the centrosymmetric phase. Our preliminary conclusion from theory was that the structural ground state of EBBO is either $P3$ or $P6_3$ (see Fig. 1(c) and (d)). Both structures exhibit very similar patterns of atomic displacements and very close energy. Further calculations with more accurate relaxation criteria were performed to distinguish the true ground state but they led to even smaller energy differences. In the $P3$ or $P6_3$, the atomic displacement breaking centrosymmetry is due to barium moving in an oxygen environment along the *c* axis (Fig. 1(c) and (d)). Interestingly, in the $P\bar{1}$ structure, which is only marginally higher in energy than the $P3$ and $P6_3$ phases, the barium displacement pattern is antipolar (Fig. 1(e)). The presence of several phases very close in energy is the signature of a flat potential energy landscape. In all phases, the Eu and the metaborate B_3O_6 group do not move significantly. The noncentrosymmetric stable ground state indicates that this material could present a second harmonic generation response and potentially ferroelectric.

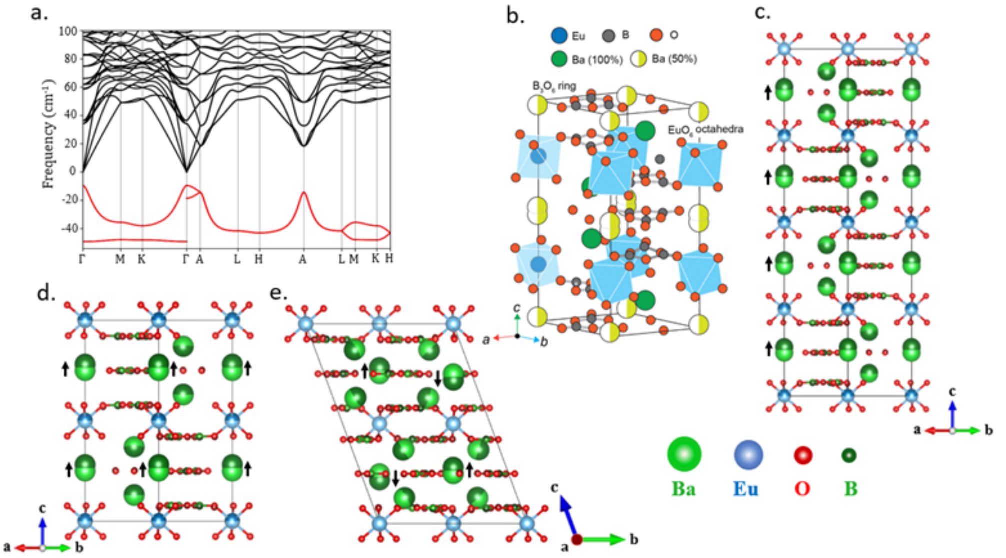

Fig. 1. (a) Phonon dispersion relations for $EuBa_3B_9O_{18}$. Unstable modes are shown in red. (b) Structure of the experimentally determined $P\bar{6}$ phase showing the displacive disorder of the barium atoms (c) Structure of the $P3$ phase showing the atomic displacements with respect to the centrosymmetric $P6_3$/m phase. The dark and clear balls represent the atoms in the $P3$ and in the $P6_3/m$ phase, respectively. (d) Same, for the $P6_3$ phase and (e) the $P\bar{1}$ phase.

Table 1. Energy difference (meV/atom) between the centrosymmetric structure ($P6_3/m$) and the different distorted structures obtained from the phonon band structure of $EuBa_3B_9O_{18}$.

$P6_3$	$P\bar{1}$	Pm	$P2_1/c$	$P2_1/m$	P3
-2.97	-2.33	2.98	-1.52	0.18	**-3.19**

3.2. Crystal synthesis and structure

Motivated by the computational results, we synthesized the polycrystalline EBBO with high purity using the solid-state reaction. The phase and phase purity were confirmed by the PXRD patterns shown in Fig. 2(a). Then the pure polycrystalline EBBO was used to synthesize the single crystals shown in Fig. 2(b) using the floating zone technique. The as-grown EBBO single crystals are transparent and stable in an ambient atmosphere for at least six months. It is also stable in various solvents such as water, alcohol, and acetone.

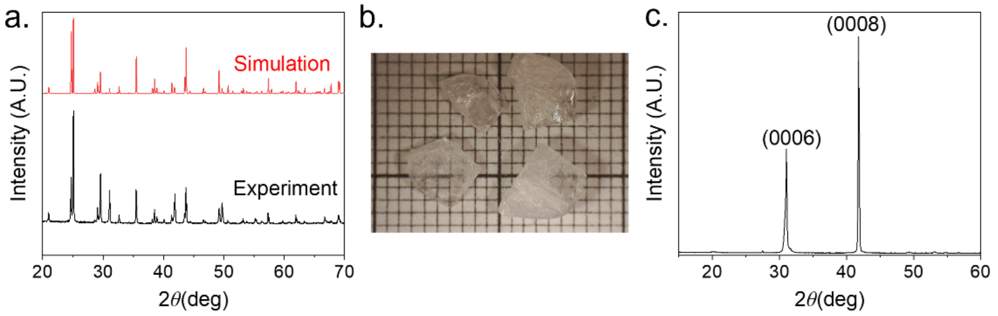

Fig. 2. (a) Powder XRD pattern of polycrystalline EBBO. (b) Optical image of EBBO crystals grown using the floating-zone technique. (c) XRD patterns measured on the surface of a representative EBBO crystal.

EBBO consists of planar metaborate [B_3O_6] rings with π-conjugated bonds, aligning parallel to each other along the [0001] direction. It also comprises EuO_6 octahedra and irregular BaO_6 and BaO_9 polyhedra, similar to the reported $YBa_3B_9O_{18}$ structure [21]. Because of its planar nature, single crystal EBBO can be easily cleaved along the (0001) plane, verified by XRD (Fig. 2(c)).

As shown later, we clearly observed the SHG response from the EBBO crystal, in agreement with the computational results suggesting the symmetry lowering from the centric $P6_3/m$ structure. To identify the detailed atomic structure experimentally, single-crystal XRD measurements were perfomed for the grown EBBO crystals on a Rigaku MicroMax 007 rotating anode (Cu) x-ray generator equipped with Osmic Varimax VHF monochromator, a universal four-circle kappa goniometer and a HyPix-Arc150 area detector. The collected diffraction dataset was refined using a structural model with $P6_3$, $P3$, and $P\bar{6}$, which are noncentrosymmetric subgroups of $P6_3$/m. The $P6_3/m$, $P6_3$, and $P\bar{6}$ have the same unit-cell size, whereas the unit cell of the $P3$ structure is doubled along the c axis, i.e., $a \times b \times 2c$ cell metric, where a, b, and c are the lattice vectors of the $P6_3/m$ structure. The reflection conditions of the four space groups are listed in Table 2.

Table 2. Reflection conditions of the space groups $P6_3/m$, $P6_3$, $P3$, and $P\bar{6}$.

	hhil	$h\bar{h}0l$	$hh\overline{2h}l$	000l
$P6_3/m$ and $P6_3$	None	None	None	$l = 2n$
$P3$	None	None	None	None
$P\bar{6}$	None	None	None	None

First, we looked for superlattice reflections representing an enlarged unit cell with respect to the $a \times b \times c$ cell metric. No superlattice reflections were, however, observed, indicating the low possibility of the $P3$ structure with the doubled unit cell. Indeed, the $P3$ model resulted in a bad fit to the collected dataset ($R_{\mathrm{int}} = 38.95\%$), and thus we excluded the space group $P3$. The dataset was then fitted with the structural model with $P6_3$ and $P\bar{6}$ symmetries. Although the $P6_3$ model led to the best fit ($R_1 = 8.81\%$), this value is very similar to that obtained through the refinement with the $P\bar{6}$ model ($R_1 = 8.85\%$). Thus, we cannot unambiguously determine the crystal structure of EBBO only via single-crystal XRD and the subsequent refinements. With the help of nonlinear optical measurements, we assigned the $P\bar{6}$ structure to EBBO (see Fig. 1(b)); the $P\bar{6}$ is the only one consistent with our SHG results (shown later), where a significant SHG signal was observed at normal incident geometry. Note that no SHG signal is expected from the $P6_3$ structure at this optical geometry. The structural parameters of the $P\bar{6}$ phase obtained from the refinement are summarized in Table S1. The refined crystal structure is depicted in Figure 1(b).

In this refinement, we applied the split-atom model for one of the Ba sites, and this treatment improved the fitting significantly. This is consistent with the symmetry-breaking shift of Ba atoms revealed by our FP calculations. Such displacive-type static disorder may cause the discrepancy in the space group symmetry between the computation and experiment. If the displacive disorder is ignored, as is often the case in FP calculations, the Ba atoms have no degree of freedom to shift under the $P\bar{6}$ symmetry, and thus the stability of the $P\bar{6}$ phase is probably underestimated. Despite such difficulties, analyzing unstable phonons is an effective means to search for hidden noncentrosymmetric materials as showcased in this research.

3.3. Linear optical properties

To understand the lower limit of the spectral range in which EBBO is applicable, we investigated its short-cutoff wavelength using both UV-Vis spectroscopy and ellipsometry. UV-Vis transmittance was collected on the (0001) plane of a single crystal EBBO with a thickness of ~500 µm (Fig. 3(a)). In addition, the absorption coefficient α was extracted from ellipsometry data measured on a polycrystalline pellet as shown in the inset of Fig. 3(b). Both the UV-Vis transmittance and ellipsometry data yielded the same short-cutoff wavelength of ~250 nm.

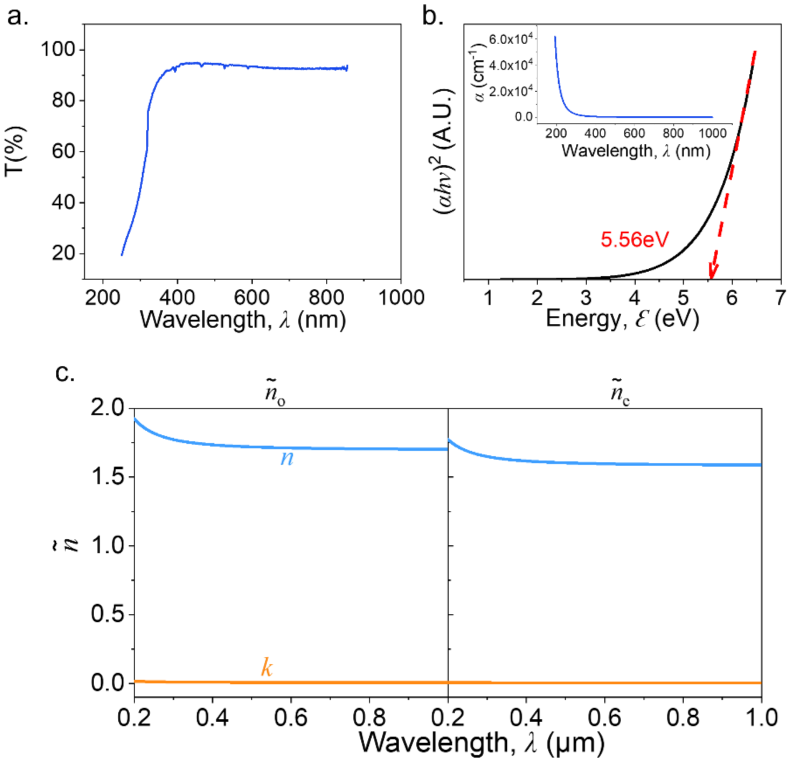

Fig. 3. (a) Transmittance spectrum of a single crystal EBBO. (b) Tauc plot of EBBO, indicating a direct bandgap of 5.56 eV. Inset: Absorption coefficient of EBBO obtained from a polycrystalline pellet using ellipsometry. (c) The complex ordinary and extraordinary refractive index of EBBO. The blue and orange curves represent the real and imaginary components, respectively.

The bandgap of the crystal was extracted by the Tauc analysis $(\alpha h\nu)^{1/n} = A(h\nu - E_g)$, in which n equals 0.5 and 2 for direct and indirect bandgap, respectively [11]. By plotting the Tauc plots for both direct and indirect bandgaps, we found that the better fit was the direct bandgap, which was 5.56 eV, as shown in Fig. 3(b).

To extract the complex ordinary and extraordinary refractive indices, we performed spectroscopic ellipsometry at room temperature on a single crystal in three crystal orientations: [0001]//lab X, [0001]//lab Y and [0001]//lab Z. The three sets of ellipsometry spectra were fitted simultaneously to the Cauchy equation $n = A + \frac{B}{\lambda^2} + \frac{C}{\lambda^4}$ for the real part and Urbach absorption equation $k = k_0 e^{(E-E_o)/E_u}$ for the imaginary part of the anisotropic refractive indices, as seen in Fig. 3(c). The parameters of the Cauchy equations and Urbach absorption equations are shown in Table 3 and Table 4.

Table 3. The parameters of Cauchy equations for anisotropic refractive indices.

n	A	B (μm^2)	C (μm^4)
n_o	1.697	0.00506	1.6234×10^{-4}
n_e	1.583	0.00467	1.1898×10^{-4}

Table 4. The parameters of Urbach absorption equations for imaginary refractive index.

k	k_0	E_u (eV)	E_0 (eV)
k_o	0.11911	2.825	4.96
k_e	0.02883	3.472	4.96

3.4. Second harmonic generation

Second harmonic generation (SHG) is a process combining two photons of frequency ω into one photon of frequency 2ω through a noncentrosymmetric material. For real applications, the SHG process should take place only from the ground state to the virtual states to ensure minimal absorption and a non-resonant process. In the case of EBBO, the bandgap is 5.56 eV (~220 nm); therefore fundamental wavelength needs to be longer than 440 nm. The wavelength demonstrated here was 800 nm, and the wavelength of the SHG was 400 nm.

The SHG measurement was performed in normal reflection geometry with a nonlinear optical microscope, shown in Fig. 4(a). The fundamental laser beam was linearly polarized and rotated by an angle of ψ using a halfwave plate, and the SHG light was decomposed into p-polarized (||) and s-polarized (⊥) SHG light and detected by a photomultiplier tube.

Since the crystal belongs to the hexagonal crystal system, its crystal physics coordinate (Z_1, Z_2, Z_3) is defined as Z_1//[$2\bar{1}\bar{1}0$], Z_2//[$01\bar{1}0$], Z_3//[0001]. The crystal was oriented such that -Z_2 and Z_1 axes were parallel to the lab axes X and Y, respectively.

A significant SHG signal indicates the absence of the inversion symmetry, in consistent with our FP calculations result. The observation of SHG signal in normal incidence rules out the $P6_3$ space group since point group 6 should not show any SHG signal when the incidence beam is along the 6-fold axis. This fact combined with the x-ray analysis presented earlier points to the $P\bar{6}$ as the most likely space group for this crystal. To obtain the d_{ij} coefficients ratios of EBBO, the polar plots were fitted to an analytical model based on its point group symmetry $\bar{6}$ and compared with that measured on a wedged z-cut $LiNbO_3$ reference under the same experimental conditions.

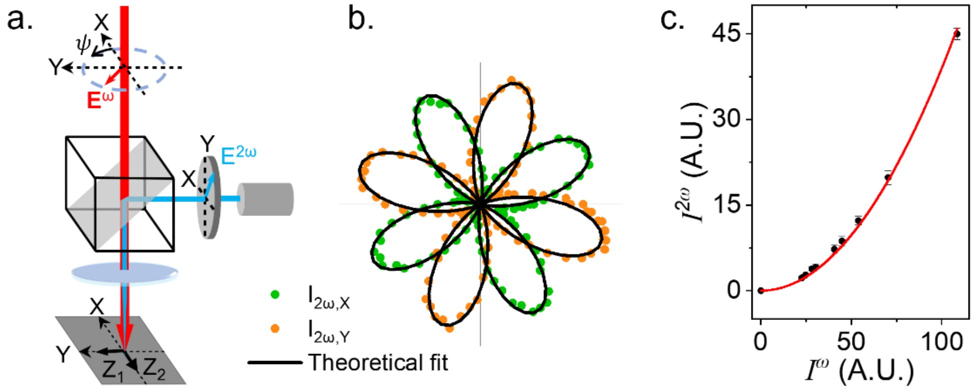

Fig. 4. (a) Schematic of the SHG polarimetry geometry. (b) Polar plots of *p*-polarized (a) and *s*-polarized (b) SHG intensities measured in normal reflection geometry at 800 nm fundamental wavelength for extracting the ratio of d_{11}/d_{22} and the absolute values. The black curves are the theoretical fit based on point group $\bar{6}$. (c) SHG power dependency of EBBO crystal, confirming the detected signal was generated from the SHG process.

The theoretical expressions for the SHG intensity at normal incidence can thus be expressed as

$$\begin{aligned} I_{\parallel}^{2\omega} &\propto (d_{11}\sin 2\psi + d_{22}\cos 2\psi)^2 \\ I_{\perp}^{2\omega} &\propto (-d_{11}\cos 2\psi + d_{22}\sin 2\psi)^2. \end{aligned} \tag{1}$$

The two non-zero SHG coefficients, d_{11} and d_{22}, could both be probed using the chosen geometry. The ratio of the SHG coefficients d_{11} with respect to d_{22} was extracted by fitting the SHG polar plots to Eq. (2), as shown in Fig. 4(b). The theoretical fit yielded the result of $d_{11}/d_{22} = 1.47 \pm 0.04$. By comparing the SHG intensity with that of a *z*-cut $LiNbO_3$ reference measured under the same experimental conditions (details are provided in the Supplement 1 and Code 1) [22], one can extract that $|d_{11}| = 0.52 \pm 0.03$ pm/V and $|d_{22}| = 0.35 \pm 0.02$ pm/V. In particular note that d_{11} and d_{22} share the same sign.

To ensure that the detected signal was from the second-order NLO effect, the SHG intensities were measured as a function of incident power, shown in Fig. 4(c). The solid red line is the quadratic fit, and the black dots are the experimental data. The SHG response demonstrates a clear quadratic dependence on the input power, confirming that the measured signal was generated by the second-order NLO effect.

3.5. Phase matching conditions

To obtain efficient frequency conversion, phase-matching is one of the most important criteria. The phase-matching conditions can be calculated using the Cauchy equations. From the previous section, we know that EBBO is a negative uniaxial crystal ($n_o > n_e$). Therefore, the Type I phase-matching condition is achieved when $n_{o,\omega} = n_{e,2\omega}(\theta_m)$ and $n_o^{\omega} + n_e^{\omega}(\theta_m) = 2n_e^{2\omega}(\theta_m)$ for Type II. We found that EBBO can be both Type I and Type II phase-matched, as shown in Fig. 5(a) and (b). We introduce an angle φ as the azimuthal angle, as defined in Fig. 5(c). For fundamental light of 800 nm, the effective *d* coefficients, d_{eff}, for both conditions can be expressed as

$$\begin{aligned} d_{eff,I} &= d_{11}\cos\theta_m\cos 3\phi - d_{22}\cos\theta_m\sin 3\phi + d_{31}\sin\theta_m \\ d_{eff,II} &= d_{11}\cos^2\theta_m\sin 3\phi + d_{22}\cos^2\theta_m\cos 3\phi. \end{aligned} \tag{2}$$

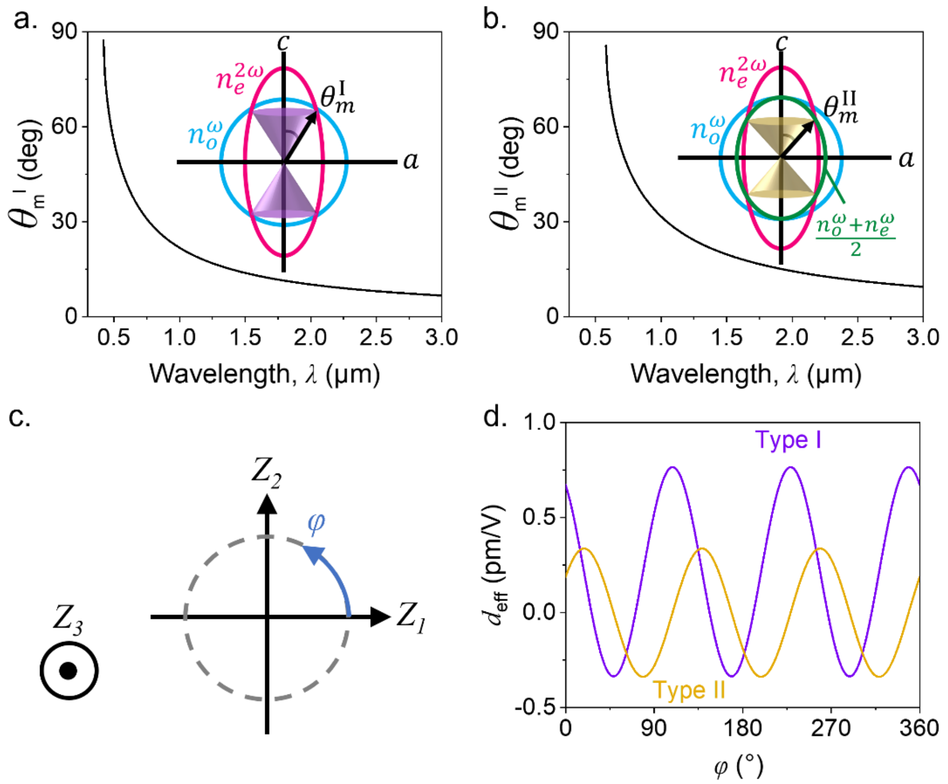

Fig. 5. Type I (a) and Type II (b) phase-matching angles as a function of wavelength. (c) definition of φ. (d) d_{eff} for Type I and Type II phase-matching conditions as a function of φ at 800 nm fundamental wavelength.

The value of d_{31} can be estimated to be 0.45 pm/V using Miller's rule, assuming that the Miller's coefficient defined as $\delta = \frac{\chi_{\omega}^{(2)}}{\chi_{2\omega}^{(1)}\left(\chi_{\omega}^{(1)}\right)^2}$ is the same as d_{11}. The maximal $|d_{\mathrm{eff,\,I}}|$ is 0.77 pm/V at $\varphi = 108.7°$ and $|d_{\mathrm{eff,\,II}}|$ is 0.34 pm/V at $\varphi = 8.3°$ (Fig. 5(d)). These are estimates assuming that Miller's rule applies; this assumption requires a more careful future testing.

4. Conclusions

We identify EBBO as a potential new noncentrosymmetric material by analyzing unstable phonons from first principles computations in the reported centrosymmetric ($P6_3/m$) structure. The inversion symmetry breaking is confirmed experimentally through SHG measurement, which confirms that the previous reported structure was incorrect [10]. Combining theory and experiment, we identify EBBO's space group to be $P\bar{6}$. Moreover, we report the first successful single crystal synthesis of EBBO using the floating-zone method. The anisotropic linear and nonlinear optical properties have been systematically characterized. It is also Type I and Type II phase-matchable in a wide range of wavelengths. FP calculations are performed to determine the most stable structure. This work suggests that rare earth metal borates are a good material system for UV NLO crystal exploration. It also shows how crystal structure previously reported to be centrosymmetric can be identified to be in fact noncentrosymmetric in first principles high-throughput phonon databases. This approach is of interest for the identification of new materials with NLO or ferroelectric properties. The point group $\bar{6}$ is non-polar. Nonetheless, motivated by the theoretical calculations, attempts were made to measure the ferroelectric hysteresis loop, which were unsuccessful as expected.

Funding. National Institutes of Health (1S10OD028589-01, 1S10RR023439-01); U.S. Department of Energy (DE-AC02-05-CH11231); National Science Foundation (1548562, DMR-2011839, DMR-2039351, DMR-2210933).

Acknowledgments. JH and VG acknowledge support from NSF DMR-2210933 as primary support. Support for crystal growth and characterization were provided by the National Science Foundation through the Penn State 2D Crystal Consortium-Materials Innovation Platform (2DCC-MIP) under NSF cooperative agreements DMR-2039351. The powder synthesis effort was supported by the National Science Foundation through the Penn State Materials Research Science and Engineering Center (MRSEC) DMR 2011839. GH acknowledges the U.S. Department of Energy, Office of Science, Office of Basic Energy Sciences, Materials Sciences and Engineering Division, under Contract DE-AC02-05-CH11231: Materials Project program KC23MP. This work used EXPANSE at San Diego Supercomputer Center through allocation MAT220002 from the Extreme Science and Engineering Discovery Environment (XSEDE), which was supported by NSF grant number #1548562. X-ray Instrument funding acknowledgment: S-10 grants from National Institutes of Health under award number 1S10OD028589-01 and 1S10RR023439-01. VS acknowledges financial support from the E.E. Just summer internship program.

Disclosures. All authors declare no conflict of interest.

Data availability. Data may be obtained from the authors upon reasonable request. Data for Supplemental Table 1 in is available in Code 1 [22].

Supplemental document. See Supplement 1 for supporting content.

References

1. J. Selles, C. Brimont, G. Cassabois, P. Valvin, T. Guillet, I. Roland, Y. Zeng, X. Checoury, P. Boucaud, M. Mexis, F. Semond, and B. Gayral, "Deep-UV nitride-on-silicon microdisk lasers," Sci. Rep. **6**(1), 21650 (2016).
2. D. Cyranoski, "Materials science: China's crystal cache," Nature **457**(7232), 953–955 (2009).
3. J. Sakuma, Y. Kaneda, N. Oka, T. Ishida, K. Moriizumi, H. Kusunose, and Y. Furukawa, "Continuous-wave 193.4nm laser with 120mW output power," Opt. Lett. **40**(23), 5590–5593 (2015).
4. N. Savage, "Ultraviolet lasers," Nat. Photonics **1**(2), 83–85 (2007).
5. C. T. Chen, G. L. Wang, X. Y. Wang, and Z. Y. Xu, "Deep-UV nonlinear optical crystal $KBe_2BO_3F_2$-discovery, growth, optical properties and applications," Appl. Phys. B **97**(1), 9–25 (2009).
6. A. Sekar, U. R. Muthurakku, and K. Sivaperuman, "An overview on recent trends in deep-ultraviolet (DUV) and ultraviolet (UV) nonlinear optical crystals," ChemistrySelect **6**(39), 10688–10716 (2021).
7. R. Arun Kumar, M. Arivanandhan, and Y. Hayakawa, "Recent advances in rare earth-based borate single crystals: potential materials for nonlinear optical and laser applications," Prog. Cryst. Growth Charact. Mater. **59**(3), 113–132 (2013).
8. R. Liu, H. Wu, H. Yu, Z. Hu, J. Wang, and Y. Wu, "$K_5Mg_2La_3(BO_3)_6$: an efficient, deep-ultraviolet nonlinear optical material," Chem. Mater. **33**(11), 4240–4246 (2021).
9. W. Liu, M.-H. Lee, R. Guo, and J. Yao, "Two non-centrosymmetric mixed alkali metal and alkaline earth metal scandium borate nonlinear optical materials with short ultraviolet cutoff edges," Dalton Trans. **52**(11), 3344–3350 (2023).
10. X. Z. Li, C. Wang, X. L. Chen, H. Li, L. S. Jia, L. Wu, Y. X. Du, and Y. P. Xu, "Syntheses, thermal stability, and structure determination of the novel isostructural RBa3B9O18 (R = Y, Pr, Nd, Sm, Eu, Gd, Tb, Dy, Ho, Er, Tm, Yb)," Inorg. Chem. **43**(26), 85555–8560 (2004).
11. J. Tauc, R. Grigorovici, and A. Vancu, "Optical properties and electronic structure of amorphous germanium," Phys. Status Solidi **15**(2), 627–637 (1966).
12. A. Togo and I. Tanaka, "First principles phonon calculations in materials science," Scr. Mater. **108**, 1–5 (2015).
13. A. Togo, "First-principles phonon calculations with phonopy and phono3py," J. Phys. Soc. Jpn. **92**(1), 012001 (2023).
14. A. Jain, S. P. Ong, G. Hautier, W. Chen, W. D. Richards, S. Dacek, S. Cholia, D. Gunter, D. Skinner, G. Ceder, and K. A. Persson, "Commentary: The materials project: A materials genome approach to accelerating materials innovation," APL Mater. **1**(1), 011002 (2013).
15. G. Bergerhoff, R. Hundt, R. Sievers, and I. D. Brown, "The inorganic crystal structure data base," J. Chem. Inf. Comput. Sci. **23**(2), 66–69 (1983).
16. G. Cai, M. He, X. L. Chen, W. Y. Wang, Y. F. Lou, H. H. Chen, and J. T. Zhao, "Crystal structure and luminescence properties of a novel promising phosphor Ba3ScB9O18," Powder Diffr. **22**(4), 328–333 (2007).
17. G. Cai, X. L. Chen, W. Y. Wang, Y. F. Lou, J. Liu, J. T. Zhao, and H. H. Chen, "A new promising scintillator $Ba_3InB_9O_{18}$," J. Solid State Chem. **181**(3), 646–651 (2008).
18. C. J. Duan, W. F. Li, J. L. Yuan, and J. T. Zhao, "Synthesis, crystal structure and X-ray excited luminescent properties of $LuBa_3B_9O_{18}$," J. Alloys Compd. **458**(1-2), 536–541 (2008).
19. K. F. Garrity, "High-throughput first-principles search for new ferroelectrics," Phys. Rev. B **97**(2), 024115 (2018).

20. M. Markov, L. Alaerts, H. P. Coutada Miranda, G. Petretto, W. Chen, J. George, E. Bousquet, P. Ghosez, G. M. Rignanese, and G. Hautier, "Ferroelectricity and multiferroicity in anti–Ruddlesden–Popper structures," Proc. Natl. Acad. Sci. U. S. A. **118**(17), e2026020118 (2021).
21. M. He, T. Z. Liu, J. Cai, Z. H. Zhang, and X. E. Gu, "Experimental investigation on anisotropic characteristic of $YBa_3B_9O_{18}$," Micron **89**, 16–20 (2016).
22. M. He, T. Z. Liu, J. Cai, Z. H. Zhang, and X. E. Gu, "Computationally-driven discovery of second harmonic generation in $EuBa_3(B_3O_6)_3$ through inversion symmetry breaking: code," figshare, 2023, https://doi.org/10.6084/m9.figshare.24430981.
23. G. Petretto, S. Dwaraknath, H. P. C. Miranda, D. Winston, M. Giantomassi, M. J. Van Setten, X. Gonze, K. A. Persson, M. Hautier, and G. M. Rignanese, "High-throughput density-functional perturbation theory phonons for inorganic materials," Sci. Data **5**, 1–12 (2018).